DIAGNOSTIC IMAGING QC SOLUTIONS

FROM RADIOLOGICAL IMAGING TECHNOLOGY, INC.

Radia Diagnostic performs automated phantom analysis in seconds. The simple, easy-to-use software tools provide complete scoring of all phantom parameters with precision and accuracy. All modules come equipped with tracking, trending and hands-free automation features designed to streamline your imaging QC workflow.

SPECIFIC MODULES & PHANTOMS

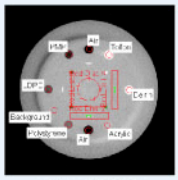

CATPHAN® 500/600 Series

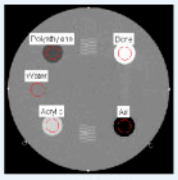

ACR CT (Gammex 464)

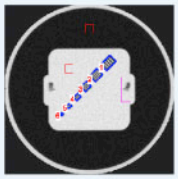

GE CT

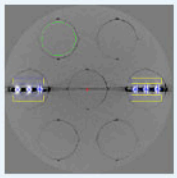

Leeds Sedentex Dental CBCT

CT/CBCT: Radia Diagnostic features the most robust and automated CT/CBCT phantom analysis on the market. Easily score vendor-supplied and ACR test phantoms with fast, quantitative, repeatable results for HU accuracy and constancy, geometric distortion, slice thickness, contrast/noise, and resolution. Analyze dental CBCT images with results for uniformity/noise, geometric distortion, high-density artifacts, low contrast detectability, and resolution.

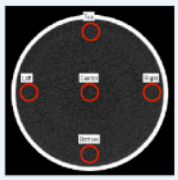

Universal CT Water Phantom: This uniformity test allows you to easily adjust the size and position of the analysis area to match any CT water phantom. This routine is perfect for daily axial and helical uniformity measurements.

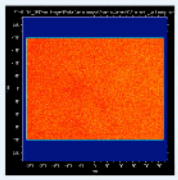

Gamma Camera: Easily measure the Intrinsic Flood Field Uniformity (NEMA NU 1-2012) parameters and perform automated analysis of integral uniformity, differential uniformity, and defective pixels for modern, rectangular gamma cameras.

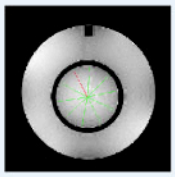

ACR MRI

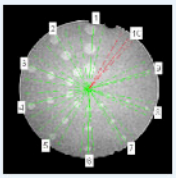

ACR Small MRI

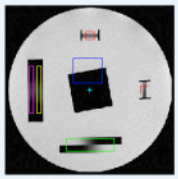

Leeds MagIQ

MRI: ACR MRI and ACR Small MRI (Extremity and Breast) phantom results are easily quantified, tracked, and reported, providing you with robust measurements for resolution, slice thickness, geometric accuracy, uniformity/noise/signal ghosting, and low contrast detectability.

Analyze Leeds MagIQ images with results for contrast, geometric distortion, resolution, slice thickness, and uniformity/noise.

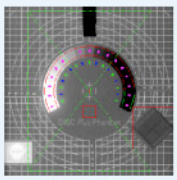

DR/CR kV: Perform all phantom parameters including contrast stepwedge, geometric accuracy, low contrast detection, MTF, noise, and uniformity. Supported phantoms include IBA Primus® L (including couch placement analysis), Leeds TOR-18 FG, PTW NORMI®-4 FLU, and DISC Plus.

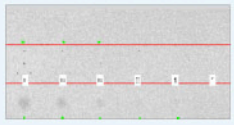

ACR FFDM: Perform complete scoring of this phantom to full requirements. Scores fibers, specs and masses to half a point. Score contrast to noise, signal to noise, and insert size.

AUTOMATION & CUSTOMIZATION FEATURES

Complete Automation: Use Cerberus to perform hands-free, automated phantom analysis. Cerberus automatically monitors folders, pin-points files, and analyzes them in the background of your machine.

Tracking & Trending: RIT*trend*™ is the all-in-one statistical database solution for all of your department's measurements. Export full reports of all imaging tests with a single click and trend results over time.

RIT*trend*™ is a trademark of Radiological Imaging Technology, Inc.

Tolerance Customization: RIT's Tolerance Manager sets tolerance values and pass/fail criteria for every measurement, and preference profiles can be precisely tailored to each individual machine in use.

CLICK TO SCHEDULE A VIRTUAL SOFTWARE DEMO TODAY!

RIT®

RADIMAGE.COM

+1.719.590.1077 // sales@radimage.com // Connect with us on social media @RIT4QA

©2021, Radiological Imaging Technology, Inc.

CATPHAN® is a registered trademark of The Phantom Laboratory. NORMI® is a registered trademark of PTW. Primus® is a registered trademark of IBA.

Check for updates

3D Inception U-net with Asymmetric Loss for Cancer Detection in Automated Breast Ultrasound

Yi Wang, Chenchen Qin, and Chuanlu Lin
National-Regional Key Technology Engineering Laboratory for Medical Ultrasound, Guangdong Key Laboratory for Biomedical Measurements and Ultrasound Imaging, School of Biomedical Engineering, Health Science Center, Shenzhen University, Shenzhen 518060, China

Di Lin
The College of Intelligence and Computing, Tianjin University, Tianjin 300354, China

Min Xu and Xiao Luo
Department of Ultrasound, Sun Yat-Sen University Cancer Center, State Key Laboratory of Oncology in South China, Collaborative Innovation Center for Cancer Medicine, Guangzhou 510060, China

Tianfu Wang
National-Regional Key Technology Engineering Laboratory for Medical Ultrasound, Guangdong Key Laboratory for Biomedical Measurements and Ultrasound Imaging, School of Biomedical Engineering, Health Science Center, Shenzhen University, Shenzhen 518060, China

Anhua Li
Department of Ultrasound, Sun Yat-Sen University Cancer Center, State Key Laboratory of Oncology in South China, Collaborative Innovation Center for Cancer Medicine, Guangzhou 510060, China

Dong Ni[a)]
National-Regional Key Technology Engineering Laboratory for Medical Ultrasound, Guangdong Key Laboratory for Biomedical Measurements and Ultrasound Imaging, School of Biomedical Engineering, Health Science Center, Shenzhen University, Shenzhen 518060, China

(Received 2 January 2020; revised 3 July 2020; accepted for publication 6 July 2020; published 13 October 2020)

Purpose: Breast cancer is the most common cancer and the leading cause of cancer-related deaths for women all over the world. Recently, automated breast ultrasound (ABUS) has become a new and promising screening modality for whole breast examination. However, reviewing volumetric ABUS is time-consuming and lesions could be missed during the examination. Therefore, computer-aided cancer detection in ABUS volume is extremely expected to help clinician for the breast cancer screening.
Methods: We develop a novel end-to-end 3D convolutional network for automated cancer detection in ABUS volume, in order to accelerate reviewing and meanwhile to provide high detection sensitivity with low false positives (FPs). Specifically, an efficient 3D Inception Unet-style architecture with fusion deep supervision mechanism is proposed to attain decent detection performance. In addition, a novel asymmetric loss is designed to help the network balancing false positive and false negative regions, thus improving detection sensitivity for small cancerous lesions.
Results: The efficacy of our network was extensively validated on a dataset including 196 patients with 661 cancer regions. Our network obtained a detection sensitivity of 95.1% with 3.0 FPs per ABUS volume. Furthermore, the average inference time of the network was 0.1 second per volume, which largely shortens the conventional reviewing time.
Conclusions: The proposed network provides efficient and accurate cancer detection scheme using ABUS volume, and may assist clinicians for more efficient breast cancer screening. © *2020 American Association of Physicists in Medicine* [https://doi.org/10.1002/mp.14389]

Key words: automated breast ultrasound (ABUS), breast cancer, computer-aided detection, convolutional neural networks

1. INTRODUCTION

Breast cancer is the most common cancer and the leading cause of cancer-related deaths for women all over the world.[1] Early screening and treatment of breast cancer have been shown to be useful in reducing mortality rates.[2] Currently mammography and breast ultrasound are two popular modalities for the screening of breast tumor.[3] Although mammography is the primary imaging tool for screening, it suffers from the limitation of insensitivity for women with dense breast tissue.[4] As an adjunct imaging modality to mammography, the breast ultrasound improves the screening sensitivity in dense breasts.[5] However, conventional two-dimensional (2D) handheld ultrasound is operator-dependent and cannot visualize the whole breast. To alleviate the drawbacks of conventional ultrasound, automated breast

ultrasound (ABUS) has been developed to automatically scan the whole breast and provide 3D views of the breast from the skin line to the chest wall (see Fig. 1). However, reviewing ABUS images is extremely time-consuming, and the relatively high false positive rate remains a concern (Fig. 2). Therefore, the computer-aided detection (CADe) in ABUS images is expected to assist clinicians in facilitating the identification of breast cancer lesions.

In the last decade, a number of CADe methods for breast cancer screening have been proposed. One main methodological category is low-level image processing based scheme. Ikedo et al.[6] employed the Canny edge detector and watershed algorithm to identify mass candidate regions. The detection sensitivity was 80.6% with 3.8 false positives (FPs) per whole breast image on a dataset of 36 masses (15 cysts, 5 fibroadenomas, and 16 malignant masses). Chang et al.[7] utilized gray level slicing method to merge pixels with similar intensities and divide ultrasound images into several regions. Then a set of computerized features were calculated to determine whether or not each region was a part of a tumor. The detection sensitivity of this CADe system was 92.3% with 1.76 FPs per case on a dataset of 25 patients with 26 lesions. Such image processing methods were easy to be implemented; however, they required very strong prior knowledge on intensity distribution, which may probably result in a reduced sensitivity when the image quality is not good enough. In contrast, traditional machine learning methods have been widely investigated, as another methodological stream, to analyze the ABUS images using various hand-crafted features. Tan et al.[8] calculated several voxel features such as water droplets, sawtooth, contrast, depth, etc., and further used a GentleBoost cascade classifier to detect tumor regions. Although the FP per ABUS volume was <1; the sensitivity was only 64% on a dataset including 323 breast lesions. Moon et al.[9] employed fuzzy C-means clustering to extract abnormal regions, then quantified seven echogenicity/morphology-related features and used a logistic regression classifier to filter out the FP regions. The sensitivity was 89.19% with 2.0 FPs per volume on a dataset including 148 tumor lesions. Ye et al.[10] used 3D geodesic active contours to segment candidate regions and applied support vector machine to discriminate real breast masses. The detection sensitivity were 95%, 90%, and 70% with 4.3, 3.8, and 1.6 FPs per volume, respectively, on a dataset including 51 ABUS volumes with 44 breast masses. Kozegar et al.[11] utilized an ensemble classification method to classify the cancer regions and achieved region-based sensitivity of 68% at 1 FP per ABUS image. It is worth noting that most traditional classification-based methods had complicated pipelines and required substantial hand-crafted features.

Recently, deep learning methods have become dominant over traditional CADe approaches.[12] Yap et al.[13] studied several conventional deep models (e.g., 2D Unet[14], LeNet[15] and FCN-AlexNet[16]) for breast lesion detection in 2D ultrasound

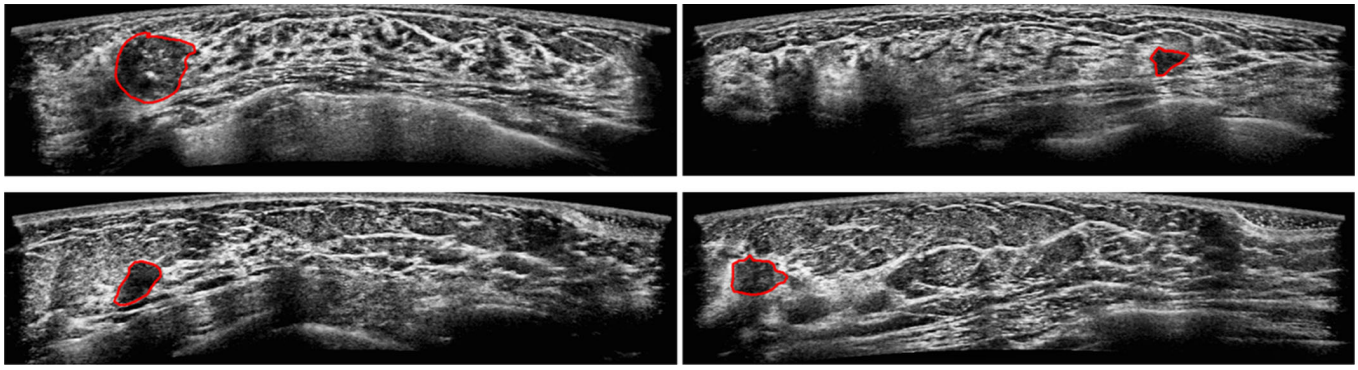

FIG. 1. Automated breast ultrasound (ABUS) images. Red contours indicate cancer regions annotated by a clinician. Cancers have large intraclass appearance variations. [Color figure can be viewed at wileyonlinelibrary.com]

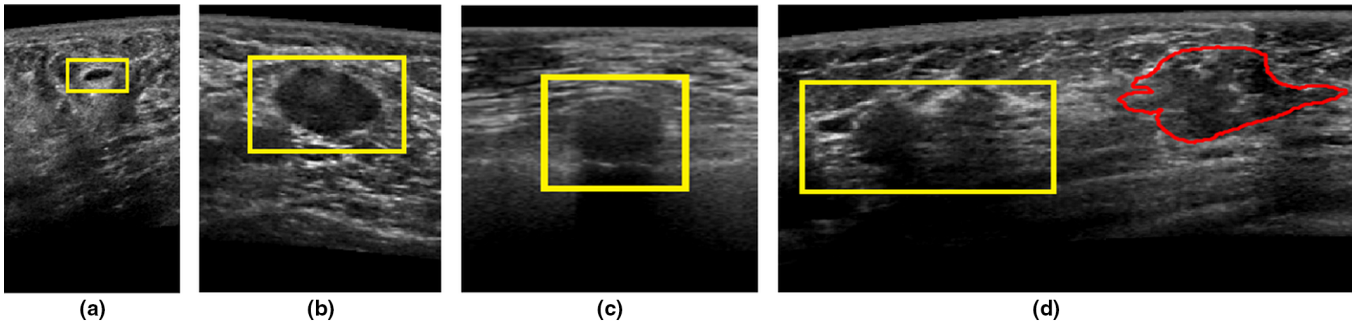

FIG. 2. Common cancer false positive types: (a) vascular dilatation due to the compression from neighboring lesion, (b) hydatoncus, (c) shadow caused by ribs, (d) shadow caused by the mammary gland, red contour denotes a biopsy-proven cancer region. [Color figure can be viewed at wileyonlinelibrary.com]

images. Validated on two 2D ultrasound datasets with 306 and 163 images, the detection sensitivities were 98% and 92% with FPs per image of 0.16 and 0.17, respectively. However, directly employing these 2D convolutional neural networks (CNNs) to perform cancer detection in ABUS volumes cannot effectively leverage the 3D information provided by ABUS data, thus may not guarantee satisfactory sensitivity and FPs. Our previous work[17] proposed a 3D CNN architecture for cancer detection in ABUS volumes. A densely deep supervision mechanism was introduced to augment the detection sensitivity. To meanwhile control the FPs, a threshold map layer was implemented in the network to adaptively distinguish cancer and non-cancer regions. The detection sensitivity was 93% at 2.2 FPs per ABUS volume, on a dataset of 196 patients with 661 cancer regions. Although the proposed CADe network can provide high sensitivity and low false positives, it poses challenges of huge computation and network parameters. The previous network took averagely 1 min to automatically review an ABUS volume; the reviewing procedure is efficiently accelerated in this study, which is more clinically practical to facilitate the CADe for breast cancer.

For this study, we offer an innovative end-to-end 3D convolutional network for automated cancer detection in ABUS, in order to accelerate reviewing and meanwhile to provide high detection sensitivity with low FPs. Our contribution is twofold. First, we develop an efficient 3D Inception Unet-style CNN with fusion deep supervision mechanism. Inspired by decomposition of convolution kernel in Inception V2,[18] we design inception CNN blocks which fuse 2D and 3D convolution operations. The proposed CNN blocks allow our network maintaining a decent detection performance and also significantly reducing parameters of the conventional 3D Unet. Second, we propose a novel asymmetric loss (AL) to help the CNN balancing false positive and false negative regions. The proposed AL is effective in solving the missing issue of small cancerous regions, thus improving detection sensitivity. The efficacy of our network was extensively validated on a dataset including 196 patients with 661 cancer regions.

The rest of this article is described as follows. Section 2 introduces the specific details of the proposed 3D inception Unet with asymmetric loss. Section 3 shows the detection performance of our method. Sections 4 and 5 present the discussion and conclusion of this study, respectively.

2. MATERIALS AND METHODS

The proposed 3D inception Unet for cancer detection in ABUS is illustrated in Fig. 3. Based on the performance analysis of conventional 3D Unet,[19] it is demonstrated that the first few layers consume the most GPU memory. To alleviate the GPU burden, we use stride convolution (stride = 2) in the first layer. Every convolution block includes a Conv3D, batch normalization (BN), and Relu layer. The construction of our 3D inception Unet involves two types of inception blocks and multiple deep supervised branches. In the expansive path of the Unet architecture, each concatenation operator has 2 inputs. The concatenated features (orange) at each upsampling level are sent to following upsampling block (gray arrow) and also to deep supervision block (orange arrow). The deep supervision blocks fuse low-level (LL) and high-level (HL) features for better prediction.

The following subsections describe the proposed network's details, and present the fusion deep supervision mechanism and the novel asymmetric loss.

2.A. 3D Inception Unet

The 3D CNN has been widely applied in video processing, such as segmentation and classification.[20,21] Nevertheless, most 3D networks pose challenges of huge computation load and number of parameters (e.g., C3D[22] has 8 layers but with about 28M parameters). Inspired by decomposition of convolution kernel in Inception V2,[18] here, we design a new 3D inception block to address above issue. Different from processing the image sequence in video [23], all three dimensions in medical volumes are relevant. Therefore, we design

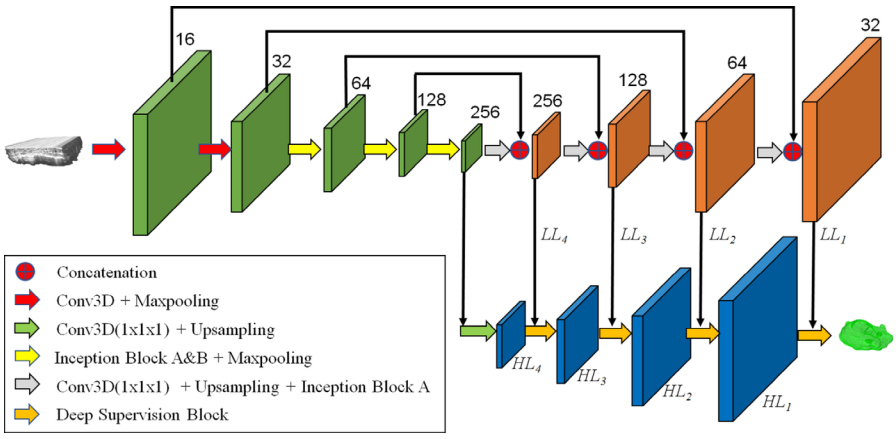

FIG. 3. The schematic overview of the proposed 3D inception Unet. The designed network involves two types of inception blocks (see details in Section 1), and multiple deep supervised branches which fuse low-level (LL) and high-level (HL) features (see details in Section 2). Note that Conv3D is a convolution operator with 3 × 3 × 3 kernel and followed by a batch normalization and Relu layer. In the first Conv3D layer, *stride* = 2. [Color figure can be viewed at wileyonlinelibrary.com]

two novel multi-function convolution blocks, Inception Block A and Inception Block B as illustrated in Figs. 4 and 5 respectively, to mimic the radiologist's perspective of reading volumes in three planes. In the type A, we use 5 groups of 3D convolution units. Specifically, $1 \times 1 \times 1$ convolution unit is used to reduce channels of features and extract point-wise features; $1 \times 1 \times 3$, $1 \times 3 \times 1$, and $3 \times 1 \times 1$ convolution units are used to extract line-wise features; $1 \times 3 \times 3$, $3 \times 1 \times 3$, and $3 \times 3 \times 1$ convolution units are introduced to extract plane-wise features; and a few $3 \times 3 \times 3$ 3D convolution units are employed as supplement to exact 3D features. Since the size of the decomposed convolution kernel is equivalent to the size of 2D convolution, the network does not dramatically increase its parameters while increasing the depth. To further reduce network parameters, we add a B type of inception block which totally removes the $3 \times 3 \times 3$ convolution unit (Fig. 5). Note that we use residual structure in both inception blocks, by directly connecting the input to the addition block. The inception blocks A and B are equipped in the network as shown in Fig. 3. The designed inception blocks are beneficial for the network to extract abundant features and converge itself more efficiently.

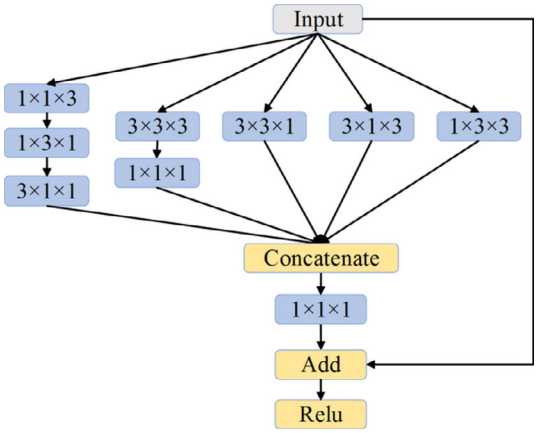

FIG. 4. Inception block A. [Color figure can be viewed at wileyonlinelibrary.com]

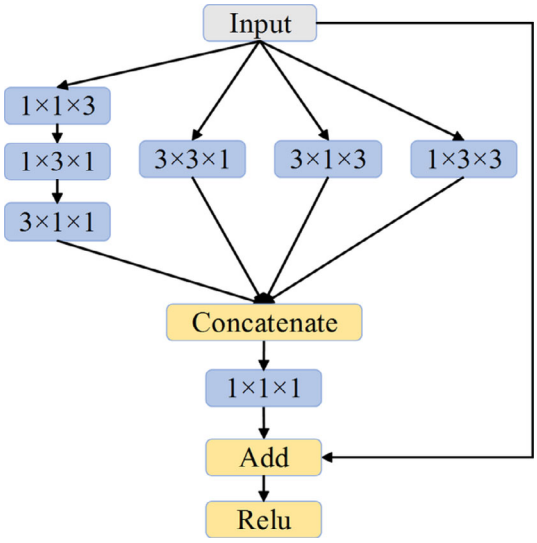

FIG. 5. Inception block B. [Color figure can be viewed at wileyonlinelibrary.com]

2.B. Fusion Deep Supervision

The Unet architecture has a downsampling path and an upsampling path. At each level of the feature map, the skip connection is used to compensate for the missing details during the downsampling procedure. In our previous work,[17] we used densely supervised branches as guidance for the cancer detection at each level and meanwhile preventing network over-fitting. However, multiple output branches corresponding to multiple loss functions would introduce lots of hyper parameters, which induces the tedious issue of hyper parameter tuning. Multiple loss functions can be calculated as follows:

$$\mathcal{L} = \sum_{i=1}^{n} \lambda_i \times aux\_loss_i, \tag{1}$$

where λ_i is the weighting parameter of the loss function aux_loss_i for the ith branch; and n is the number of total supervised branches. Tuning these hyper parameters λ_i is very time-consuming and may not achieve optimum. In this study, instead of assigning each branch a weight, we add learnable variables that can adaptively balance the weight of different branches, thus only use one loss function to supervise our network. To this end, we design a fusion deep supervision block (see Figure 6). As illustrated in Fig. 3, the deep supervision block has 2 inputs: (a) the concatenated feature maps (orange) at each upsampling level, and (b) the output of the previous deep supervision block (blue). Because of that, compared to features from previous deep supervision block, the concatenated features (orange) are from relatively shallow layer; we denote concatenated feature maps as low-level (LL) features and the other as high-level (HL) features. In our inception Unet network, we plug in fusion deep supervision blocks to fuse upsampled probability volume with low-level probability volume. Supervised information can be propagated by the highway of the fusion layer defined by the following equation:

$$F(P_i) = \sigma(f^{1\times1\times1}(P_i)), \tag{2}$$

where $P_i \in \mathbb{R}^{H\times W\times D\times C}$ is the feature map that concatenates the low-level (LL_i) and high-level (HL_i) features along channel-axis; the convolution operator of $f^{1\times1\times1}$ assigns the weight of coarse segmentation and fine segmentation probability maps adaptively; and the sigmoid activation operator σ is used to calculate the probability volume after fusion.

2.C. Asymmetric Loss

Binary cross entropy (BCE) loss and Dice loss (DSC) are usually employed for segmentation tasks.[14,17] The BCE

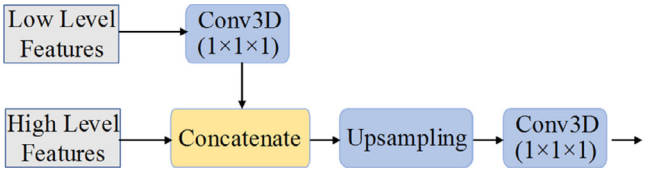

FIG. 6. Fusion deep supervision block. [Color figure can be viewed at wile yonlinelibrary.com]

loss is point-wise and may not be good at learning shape features compared to DSC loss which can be described as follows:

$$\mathbf{DSC}(A,B) = \frac{2|A \cap B|}{|A| + |B|}, \tag{3}$$

where A and B denote the predicted cancer region and the ground truth, respectively; $|A \cap B|$ denotes the intersection area of A and B. Note that when using DSC as loss, the main objective of network training is to expand the overlapped area of ground truth and predicated cancer region. Thus, the cancer region with large area would dominate the optimization procedure. For instance, suppose that there are a large cancer region and a small cancer region in one image. Then although the DSC value may be high enough, the small cancer may probably not be segmented because the DSC loss cannot balance the large cancer and small cancer. In general, the evaluation of DSC cannot reveal the real detection performance since it assigns equal weight to the false negative and false positive areas.

To address the aforementioned issue, we design an asymmetric loss (AL) to help the network balancing false positive and false negative regions. AL is defined as

$$\mathcal{L}_{al}(A,B;\alpha,\beta,\gamma) = -(1-\mathbf{T}(A,B))^{\gamma}\log(\mathbf{T}(A,B)), \tag{4}$$

where

$$\mathbf{T}(A,B) = \frac{|A \cap B|}{|A \cap B| + \alpha|A-B| + \beta|B-A|}, \tag{5}$$

where $\mathbf{T}(A, B)$ is Tversky index (TV),[24] and $|A-B|$, $|B-A|$ denote false positive area and false negative area, respectively. The TV is an asymmetric similarity measure, and can be regarded as the generalization of DSC. When $\alpha = \beta = 0.5$, TV is equivalent to DSC. By adjusting α and β, TV can pay different attention to the false positive and false negative areas. However, TV may converge to same optimum with DSC after a large number of iterations, thus inducing unsatisfactory detection performance. In order to ensure subtle cancers to be detected, we further combine focal loss[25] and TV to define the asymmetric loss, see Eq. (4). The novel AL can automatically focus on hard samples with the ability of learning shape features. AL force networks to be over-segmentation, punish under-segmentation, thus ensuring small cancers can be detected. Note that since AL may be unstable at the beginning of network training, we recommend that pre-training using DSC and then replacing DSC with AL for better results.

3. EXPERIMENTS AND RESULTS

3.A. Materials

All the experimental data were acquired from Sun Yat-Sen University Cancer Center using Invenia ABUS U-system (GE, USA). Informed consent for this retrospective study was obtained from our institutional review board. To image the whole breast, three ABUS volumes including anterior-posterior (AP), lateral (LAT), and medial (MED) passes were acquired for each breast. Therefore at least six ABUS volumes were collected for each patient. Each volume was with the voxel resolution of 0.511 mm, 0.082 mm and 0.200 mm in the transverse, sagittal and coronal sections, respectively. The size of each ABUS volume was 330 × 422 × 831.

In our experiments, ABUS volumes from 196 females (ages from 30 to 75 yr, mean 49 yr) with biopsy-proven breast cancers were acquired. From these data, 559 volumes were manually labeled by an experienced clinician using our developed annotation software. The 559 volumes contained totally 661 cancer regions (volume: $0.01 - 86.54\,\mathrm{cm}^3$, mean: $2.84\,\mathrm{cm}^3$). Fourfold cross-validation was conducted to investigate the efficacy of our detection network. As a control, 119 ABUS volumes without any abnormal findings were also involved for evaluations. Note that we randomly divided the training/testing sets by patients to avoid same one's data existing in both sets.

3.B. Evaluation Metrics

The metrics employed to evaluate detection performance included sensitivity, FPs per ABUS volume, intersection over union (IoU), and distance between centers of detected and ground truth cancers (CenDis). Sensitivity means the fraction of the cancerous lesions that are correctly detected. It is over the total number of cancerous lesions in all the ABUS volumes in the test set. Detection is considered as a true positive if the detected region has over 0.2 IoU with the ground truth. FPs per volume is the average over the falsely detected cancerous regions per ABUS volume. A better detection shall have larger values of sensitivity and IoU, meanwhile maintain lower FPs and CenDis.

3.C. Implementation Details

The proposed network was implemented with the Keras for Tensorflow.[26] Considering the burden of GPU memory, we resized each ABUS volume into the size of 256 × 128 × 256. The training augmentation included flipping, scaling, and rotation. All the training and testing were

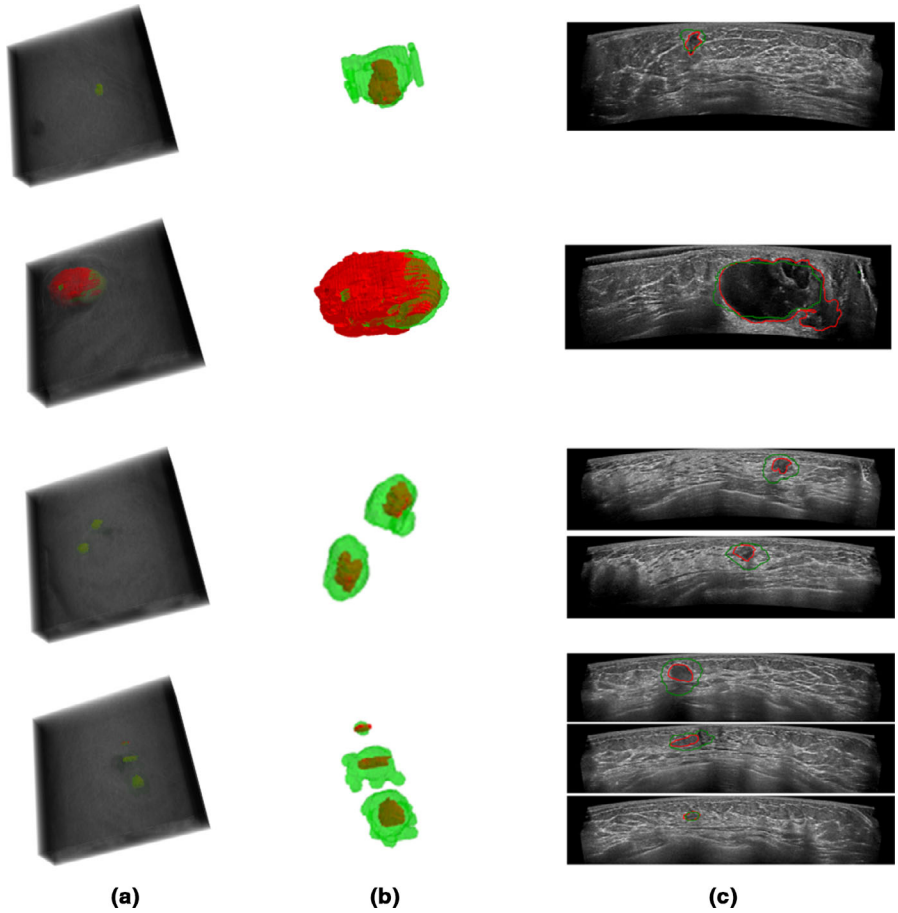

FIG. 7. Example cancer detection results obtained using our proposed network. (a) The 3D visualization of ABUS volumes with (b) annotated ground truth (red) and predicted cancer regions (green), and (c) corresponding ABUS slices illustrating ground truth (red) and correctly identified cancer regions (green). [Color figure can be viewed at wileyonlinelibrary.com]

conducted on a single NVIDIA TITAN GPU with memory of 12 GB. Adam[27] was employed to train the whole framework. In the training phase, the initial learning rate was set as 1e−3. As for the AL, $\alpha = 0.95$, $\beta = 0.05$, and $\gamma = 3$*. The training procedure stopped after 60 epochs. Note that because AL may have unstable convergence at the beginning of training, we used BraTS2015[28] to pre-train the network and then employed pre-trained weights for the initialization†. In the inference phase, the output of the network was 3D probability

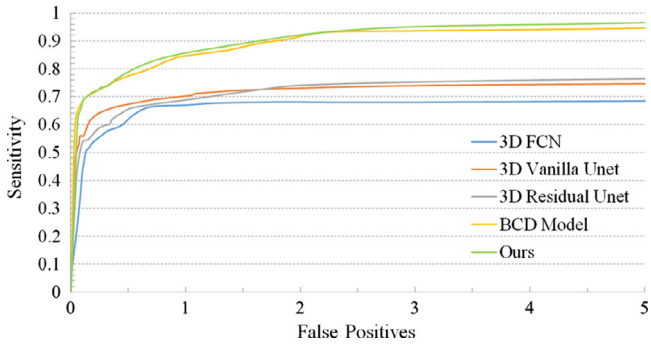

FIG. 8. The free-response receiver operating characteristic curves (FROCs) of the proposed network and compared models. [Color figure can be viewed at wileyonlinelibrary.com]

TABLE I. Numerical results of sensitivity, FPs per volume, IoU and CenDis for different networks (Mean±SD).

Method	Sensitivity (%)	FPs per volume	IoU (%)	CenDis (mm)
3D FCN[29]	67.0 ± 47.0	1.0 ± 0.9	55.4 ± 10.0	3.4 ± 1.3
3D Vanilla Unet[19]	72.2 ± 44.8	1.1 ± 1.0	56.5 ± 29.2	3.4 ± 3.2
3D Residual Unet[30]	73.8 ± 44.0	2.0 ± 1.4	53.5 ± 25.6	3.3 ± 3.0
BCD model[17]	93.0 ± 25.5	2.2 ± 2.1	49.5 ± 26.2	3.1 ± 2.2
Ours	95.1 ± 21.5	3.0 ± 1.4	60.8 ± 13.0	2.5 ± 1.6

*In our validation during implementation, we have tried (α, β) = {(0.99,0.01),(0.95,0.05),(0.90,0.10),(0.85,0.15),(0.80,0.20)}, then (α,β) = (0.95,0.05) attained satisfactory detection performance. Thus, we set $\alpha = 0.95$ and $\beta = 0.05$. As for the parameter γ, we set it empirically as 3.

†We used 274 MR volumes from BraTS2015 to pre-train the network. The pre-train was an end-to-end training. The loss function for the pre-trained was Dice loss. The reasons we used MR images to pre-train the model are as follows: (a) Compared to ultrasound images, MR images have better image quality (i.e., resolution, contrast, etc.). (b) Training using brain MR images for segmentation task would be more stable than using breast ultrasound images, because the foreground samples (i.e., cancerous regions) and background samples in ABUS images are much more unbalanced than in brain MR images.

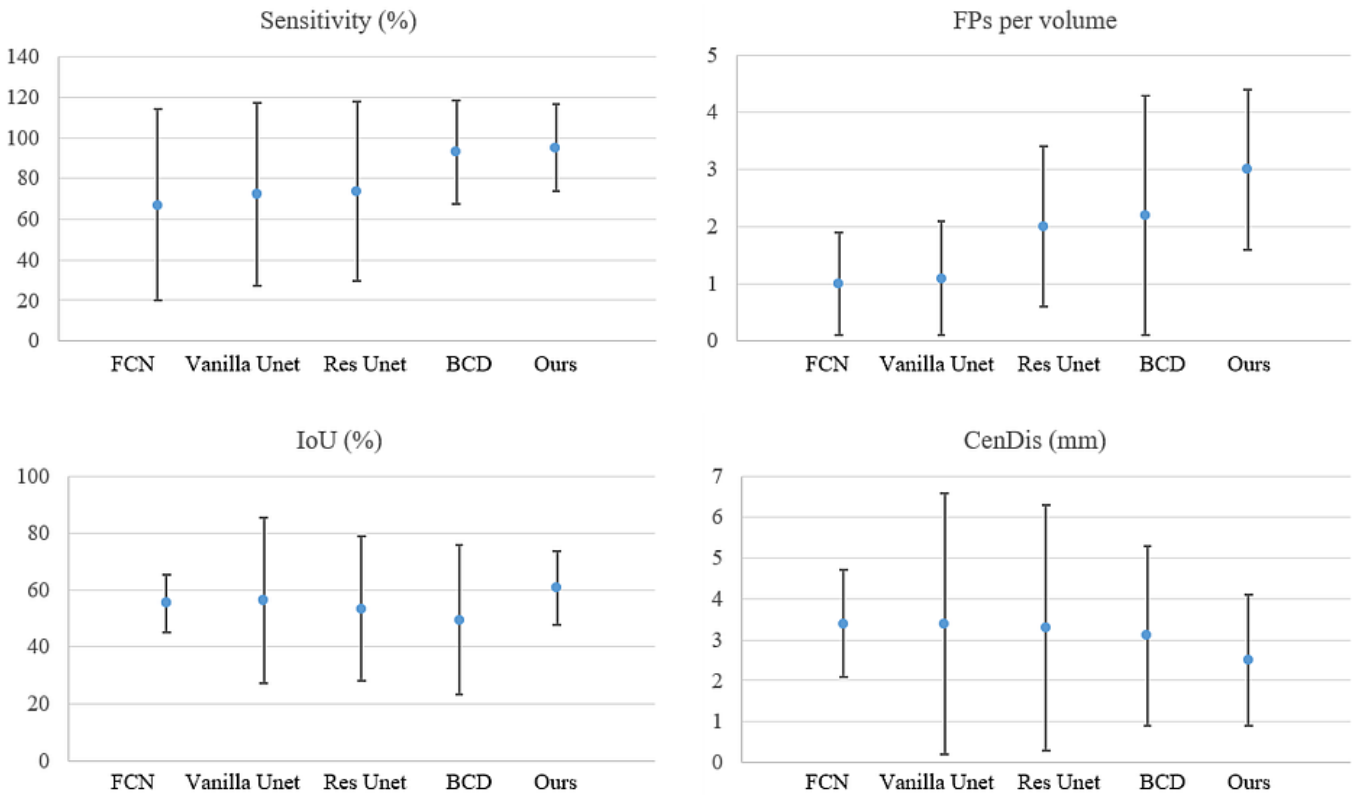

FIG. 9. The error bars of the proposed network and compared models. [Color figure can be viewed at wileyonlinelibrary.com]

volume with the range from 0 to 1 after sigmoid activation, then threshold was empirically set as 0.3 for the binarization and final prediction.

3.D. Detection Performance

Figure 7 visualizes some detection results using our proposed network. By utilizing the proposed inception blocks and asymmetric loss, our network is able to accurately predict cancerous regions. Even for those ABUS volume containing several cancerous lesions, our network can successfully detect all true positive regions.

We further extensively compared our network with the cutting-edge networks, including 3D FCN,[29] Vanilla Unet,[19] Residual Unet,[30] and our previous breast cancer detection (BCD) model.[17] Figure 8 illustrates the free-response receiver operating characteristic curves (FROCs) of the proposed network and compared models. Table I reports the numerical results of sensitivities, FPs per ABUS volume, IoU, and CenDis for different networks. Figure 9 shows the error bars of different networks. It can be observed that our network consistently outperformed other compared networks. Our network obtained a sensitivity of 95.1% with 3.0 FPs per abnormal ABUS volume[‡]. And for 119 ABUS volumes from healthy females, our network averagely generated 1.3 FPs per volume. Compared to conventional FCN and Unet, our network significantly improved detection sensitivity (with *P*-values of 1.47e−41 for 3D FCN-Ours, 4.91e−31 for 3D Vanilla Unet-Ours, and 6.84e−28 for 3D Residual Unet-Ours, respectively) and also controlled FPs at an acceptable level. Our detection sensitivity also surpassed the state-of-the-art BCD model,[17] mainly due to the design of our fusion deep supervision block and asymmetric loss. Furthermore, BCD model took 1 minute to analyze an ABUS volume. In contrast, with the effective inception blocks, our network, on the average, only spent 0.1 second for the automated cancer detection in one ABUS volume.

To demonstrate the effect of the proposed asymmetric loss, we directly compared our network with the model using conventional cross entropy (CE) loss and DSC loss, respectively. The comparison results are listed in Table II. Experimental results show the asymmetric loss outperformed CE loss and DSC loss with respect to detection sensitivity, IoU,

TABLE II. The comparison results (Mean ± SD) of our network with different loss functions.

Method	Sensitivity (%)	FPs per volume	IoU (%)	CenDis (mm)
CE loss	76.9 ± 42.2	1.9 ± 1.0	52.5 ± 31.6	3.2 ± 3.0
DSC loss	84.2 ± 36.4	2.8 ± 2.1	54.1 ± 22.3	3.1 ± 2.7
AL loss	95.1 ± 21.5	3.0 ± 1.4	60.8 ± 13.0	2.5 ± 1.6

[‡]Note that the sensitivity and specificity in classifying women with/without a breast cancer was 98.5% and 68.9%, respectively. In addition, by consolidating one's whole ABUS volumes, the sensitivity in detecting distinct cancers and FPs per person was 97.9% and 8.5 FPs per person, respectively.

and CenDis, which demonstrates the asymmetric loss contributed to the cancer detection.

Figure 10 further shows the volume distribution of all cancerous regions, and their corresponding detection sensitivities achieved by BCD model[17] and our proposed network, respectively. It is shown in Fig. 10 that our network outperformed BCD model in every different sub-ranges of cancer volume. Specifically, when cancer was larger than 1cm^3, our network achieved 100% detection rate. Even when cancer was smaller than 1cm^3, our network had a sensitivity of 87.9%.

4. DISCUSSION

Automated breast ultrasound has become a popular and promising imaging modality for the early screening of breast cancers,[31] especially in women with dense breast tissue.[32] However, reviewing an entire ABUS volume is extremely time-consuming. In this study, the automated reviewing procedure is efficiently accelerated to 0.1 s for an ABUS volume, thus is more clinically practical to facilitate the diagnosis for breast cancer. Motivated by the decomposition

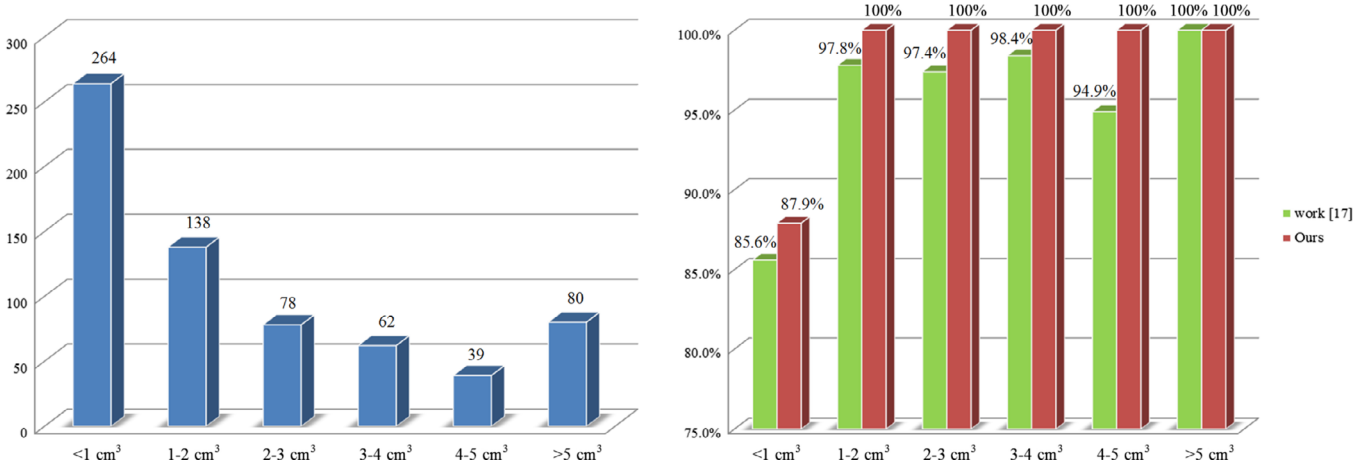

FIG. 10. Left: the volume distribution of 661 cancerous regions. Right: the detection sensitivities of the state-of-the-art BCD model[17] and our network. [Color figure can be viewed at wileyonlinelibrary.com]

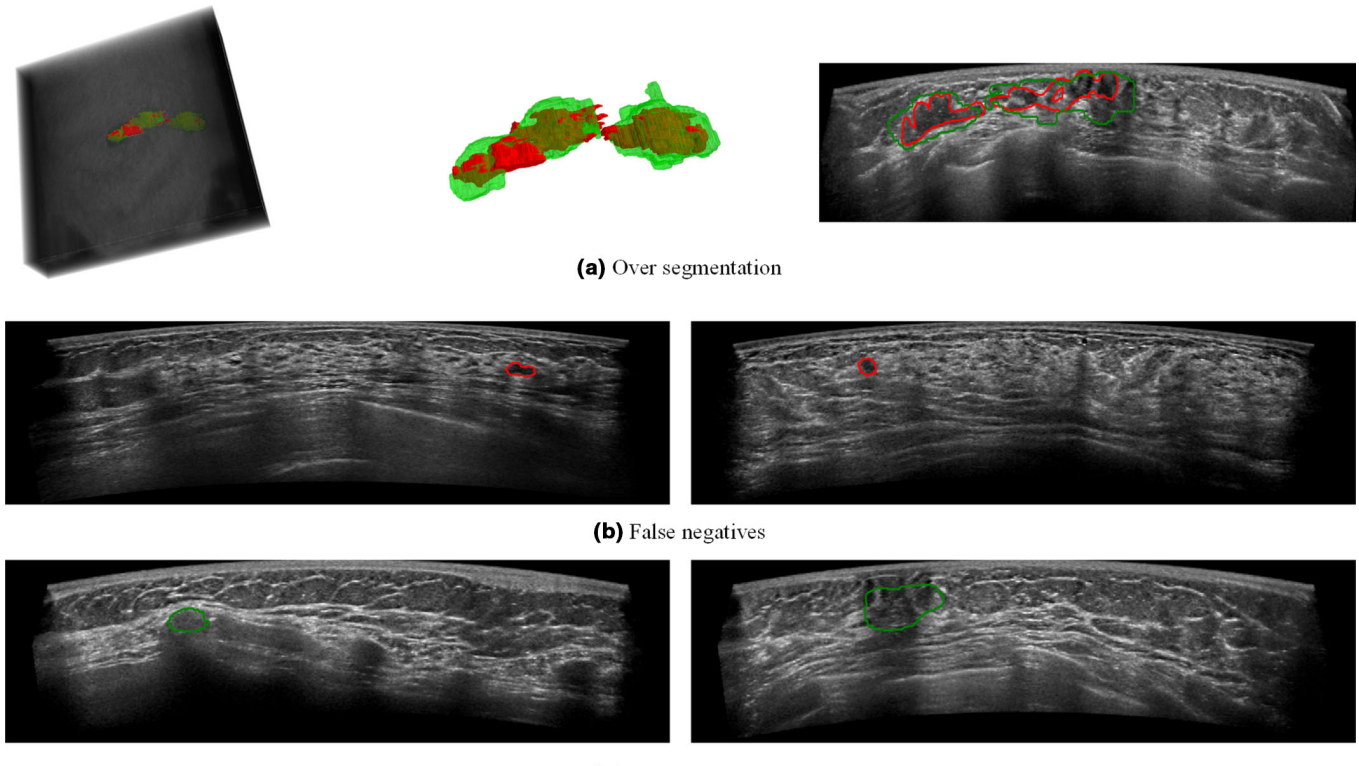

(a) Over segmentation

(b) False negatives

(c) False Positives

FIG. 11. Some failures including over segmentation, false positive/negative cases. [Color figure can be viewed at wileyonlinelibrary.com]

of convolution kernels described in Inception V2,[18] we designed inception blocks A and B as shown in Figs. 4 and 5, to significantly reduce network complexity. Moreover, the developed inception blocks fused 2D and 3D convolution operations, which followed the radiologist's routine of interpreting 3D ABUS data in three perspectives. Such design is beneficial to extract abundant features and aggregate them more efficiently. Therefore, the proposed CNN architecture is useful for accelerating screening and meanwhile maintaining a decent detection performance.

Early screening of breast cancer is proved to be helpful in reducing mortality rates.[2] Thus, the cancer detection sensitivity should be the main concern, especially for those relatively small cancerous lesions. Considering that the conventional DSC loss assigns equal weight to false negative and false positive regions, which may not be suitable for the extraction of small cancerous lesions, we utilized asymmetric loss to force networks performing over-segmentation, thus ensuring small cancers can be detected. Figure 10 demonstrates the proposed asymmetric loss is effective in identifying small cancerous regions, thus improving detection sensitivity. The numerical comparison of different loss functions in Table II also demonstrates the asymmetric loss contributes to the improvement of detection sensitivity. Nevertheless, the asymmetric loss introduces extra hyper parameters to weight the DSC index. In our current implementation, the values of most hyper parameters were set empirically, which may not be optima. Future work may focus on devising suitable loss with few or without hyper parameters. In our deep supervision scheme, we have attempted to reduce the hyper parameters used for weighting each supervision branch. To this end, we proposed a fusion deep supervision scheme, which has learnable variables that can adaptively weight different supervision branches. In such a way, multi-level features can be adaptively fused and supervision information is propagated effectively.

Although with satisfactory detection performance, our proposed CADe network still has some limitations. Figure 11 illustrates some typical failed cases including over segmentation, false positives/negatives. In order to improve the detection rate for small cancers, the asymmetric loss was used to impel the network to conduct over-segmentation. Although very effective in extracting small cancerous regions, the over-segmentation issue may fuse two close cancerous regions as one prediction, as shown in Fig. 11(a). Fortunately, the over-segmented regions contain the real cancers and could still provide useful guidance to help clinicians for the breast cancer screening. In addition, false negatives and false positives were observed in our experiments. As shown in Fig. 11(b), all undetected cancerous lesions were smaller than $1cm^3$. As for the relatively high FPs, this is mainly due to the trade-off between specificity and sensitivity. The main purpose of our method is to improve the detection sensitivity and to ensure that the detected cancer candidates can cover the real cancerous regions as much as possible, thus facilitating the further assessment by doctors. The high sensitivity would generate more FPs. The FROC results in Figure 8 show that our method achieved a sensitivity of 95%, 92%, and 86% with 3, 2, and 1 FPs per ABUS volume, respectively. In our experiments, shadows and fatty masses might be mis-identified as cancerous lesions, as illustrated in Fig. 11(c). We still have to optimize our CADe system to achieve less false negatives and false positives in the future.

5. CONCLUSIONS

In this study, we develop a novel end-to-end 3D CNN for breast cancer detection in volumetric ultrasound images. Specifically, an efficient 3D inception Unet architecture with fusion deep supervision mechanism is devised to reduce network parameters and meanwhile attaining decent detection performance. Additionally, a new asymmetric loss is designed to help the network balancing false positive and false negative regions, thus improving detection sensitivity, especially for small cancerous regions. The efficacy of the proposed network is validated on 559 cancerous ABUS volumes and 119 normal volumes. Experiments show our network has the sensitivity of 95.1% at 3.0 FPs per ABUS volume. Moreover, the average CADe time of the network is only about 0.1 s per volume. In general, the proposed network attains quite efficient and accurate detection performance, and may assist clinicians for more practical CADe in ABUS.

ACKNOWLEDGMENTS

This work was supported in part by the National Natural Science Foundation of China under Grant 61701312, in part by the Guangdong Basic and Applied Basic Research Foundation (2019A1515010847), in part by the Medical Science and Technology Foundation of Guangdong Province (B2019046), in part by the Natural Science Foundation of SZU (No. 2018010 and No. 860-000002110129), in part by the SZU Medical Young Scientists Program (No. 71201-000001), and in part by the Shenzhen Peacock Plan (KQTD2016053112051497).

CONFLICT OF INTEREST

The authors have no conflicts to disclose.

[a)]Author to whom correspondence should be addressed. Electronic mail: nidong@szu.edu.cn.

REFERENCES

1. Siegel RL, Miller KD, Jemal A. Cancer statistics, 2019. *CA: Cancer J Clin* 2019.69:7–34.
2. Jemal A, Bray F, Center MM, Ferlay J, Ward E, Forman D. Global cancer statistics. *CA: Cancer J Clin*. 2011;61:69–90.
3. Kolb TM, Lichy J, Newhouse JH. Comparison of the performance of screening mammography, physical examination, and breast us and evaluation of factors that influence them: an analysis of 27,825 patient evaluations. *Radiology*. 2002;225:165.

4. Boyd NF, Guo H, Martin LJ, et al. Mammographic density and the risk and detection of breast cancer. *N Engl J Med*. 2007;356:227–236.
5. Berg WA, Blume JD, Cormack JB, et al. Combined screening with ultrasound and mammography vs mammography alone in women at elevated risk of breast cancer. *JAMA*. 2008;299:2151–2163.
6. Ikedo Y, Fukuoka D, Hara T, et al. Development of a fully automatic scheme for detection of masses in whole breast ultrasound images. *Med Phys*. 2007;34:4378–4388.
7. Chang RF, Chang-Chien KC, Takada E, et al. Rapid image stitching and computer-aided detection for multipass automated breast ultrasound. *Med Phys*. 2010;37:2063–2073.
8. Tan T, Mordang JJ, van Zelst J, et al. Computer-aided detection of breast cancers using Haar-like features in automated 3D breast ultrasound. *Med Phys*. 2015;42:1498–1504.
9. Moon WK, Lo CM, Chen RT, et al. Tumor detection in automated breast ultrasound images using quantitative tissue clustering. *Med Phys*. 2014;41:042901.
10. Ye C, Vaidya V, Zhao F. Improved mass detection in 3D automated breast ultrasound using region based features and multi-view information. In: *36th Annual International Conference of the IEEE Engineering in Medicine and Biology Society.* IEEE; 2014:2865–2868.
11. Kozegar E, Soryani M, Behnam H, Salamati M, Tan T. Breast cancer detection in automated 3D breast ultrasound using iso-contours and cascaded RUSBoosts. *Ultrasonics*. 2017;79:68–80.
12. Shen D, Wu G, Suk GI. Deep learning in medical image analysis. *Ann Rev Biomed Eng*. 2017;19:221–248.
13. Yap MH, Pons G, Martí J, et al. Automated breast ultrasound lesions detection using convolutional neural networks. *IEEE J Biomed Health Inform*. 2017;22:1218–1226.
14. Ronneberger O, Fischer P, Brox T. U-Net: Convolutional Networks for Biomedical Image Segmentation. In: *18th International Conference of Medical Image Computing and Computer Assisted Intervention*. Berlin: Springer; 2015:234–241.
15. Lecun Y, Bottou L, Bengio Y, Haffner P. Gradient-based learning applied to document recognition. *Proc IEEE*. 1998;86:2278–2324.
16. Long J, Shelhamer E, Darrell T. Fully convolutional networks for semantic segmentation. In: *Proceedings of the IEEE Conference on Computer Vision and Pattern Recognition*. IEEE; 2015: 3431–3440.
17. Wang N, Bian C, Wang Y, et al. Densely Deep Supervised Networks with Threshold Loss for Cancer Detection in Automated Breast Ultrasound. In: *21st International Conference of Medical Image Computing and Computer Assisted Intervention*. Berlin: Springer; 2018:641–648.
18. Szegedy C, Vanhoucke V, Ioffe S, Shlens J, Wojna Z. Rethinking the Inception Architecture for Computer Vision. In: *Proceedings of the IEEE Conference on Computer Vision and Pattern Recognition*. IEEE; 2016:2818–2826.
19. Cicek O, Abdulkadir A, Lienkamp SS, Brox T, Ronneberger O. 3D U-Net: Learning Dense Volumetric Segmentation from Sparse Annotation. In: *19th International Conference of Medical Image Computing and Computer Assisted Intervention*. Berlin: Springer; 2016:424–432.
20. Socher R, Huval B, Bhat B, Manning CD, Ng A. Convolutional-Recursive Deep Learning for 3D Object Classification. *Advances in Neural Information Processing Systems*. NIPS; 2012:665-673.
21. Qi CR, Su H, Mo K, Guibas LJ. PointNet: Deep Learning on Point Sets for 3D Classification and Segmentation. In: *Proceedings of the IEEE Conference on Computer Vision and Pattern Recognition*. IEEE; 2017:652–660.
22. Du T, Bourdev L, Fergus R, Torresani L, Paluri M. Learning Spatiotemporal Features with 3D Convolutional Networks. In: *Proceedings of the IEEE International Conference on Computer Vision*. IEEE; 2015:4489–4497.
23. Qiu Z, Yao T, Tao M. Learning Spatio-Temporal Representation with Pseudo-3D Residual Networks. In: *Proceedings of the IEEE International Conference on Computer Vision*. IEEE; 2017:5534–5542.
24. Salehi SSM, Erdogmus D, Gholipour A. Tversky loss function for image segmentation using 3D fully convolutional deep networks. In: *International Workshop on Machine Learning in Medical Imaging*. Berlin: Springer; 2017:379–387.
25. Lin TY, Goyal P, Girshick R, He K, Dollar P. Focal Loss for Dense Object Detection. In: *Proceedings of the IEEE International Conference on Computer Vision*. IEEE; 2017:2980–2988.
26. Abadi M, Barham P, Chen J, et al. Tensorflow: a system for large-scale machine learning. *OSDI*. 2016;16:265–283.
27. Kingma DP, Ba J. Adam: A Method for Stochastic Optimization. arXiv:1412.6980v8; 2014.
28. Menze BH, Jakab A, Bauer S, et al. The Multimodal Brain Tumor Image Segmentation Benchmark (BRATS). *IEEE Trans Med Imaging* 2015;34:1993–2024.
29. Nie D, Cao X, Gao Y, Wang L, Shen D. Estimating CT image from MRI data using 3D fully convolutional networks. In: *Deep Learning and Data Labeling for Medical Applications*. Berlin: Springer; 2016:170–178.
30. Yu L, Yang X, Chen H, Qin J, Heng PA. Volumetric convnets with mixed residual connections for automated prostate segmentation from 3D MR images. In: *Proceedings of the Thirty-first AAAI conference on Artificial Intelligence*. AAAI; 2017:1–7.
31. Brem RF, Lenihan MJ, Lieberman J, Torrente J. Screening breast ultrasound: past, present, and future. *Am J Roentgenol*. 2015;204:234–240.
32. Brem RF, Tabár L, Duffy SW, et al. Assessing improvement in detection of breast cancer with three-dimensional automated breast US in women with dense breast tissue: the SomoInsight Study. *Radiology* 2014;274: 663–673.